INORGANIC CHEMISTRY
FRONTIERS

RESEARCH ARTICLE

View Article Online
View Journal | View Issue

Cite this: *Inorg. Chem. Front.*, 2026, **13**, 1097

Spatial construction of Pd and MnO_x on a facet-engineered $BiVO_4$ photocatalyst for efficient removal of glyphosate pesticide

Nengcong Yang,†[a] Lulu Liu,†[a] Yue Chen,†[a] Mengmeng Liu,[a] Zhian Chen,[a] Ruyan Hou, *[a] Sheng Ye *[a] and Rengui Li *[b]

As a widely used organophosphorus pesticide, glyphosate in aquatic environments and soil is causing increasing risks to public health and the environment, and feasible solutions to eliminate glyphosate contaminants are still in demand. Herein, we report on the photocatalytic removal of glyphosate using a decahedron bismuth vanadate ($BiVO_4$) photocatalyst by incorporating Pd and MnO_x cocatalysts on different exposed facets. It is elucidated that the selective deposition of Pd on the electron-accumulating {010} facets of $BiVO_4$ substantially enhances the oxygen reduction reaction, thereby accelerating the formation of $^{\bullet}O_2^-$ radicals. Concurrently, the construction of MnO_x on the hole-accumulating {110} facets promotes the water oxidation reaction, augmenting the production of $^{\bullet}OH$ radicals. The synergistic integration of Pd and MnO_x dual cocatalysts onto different facets of $BiVO_4$ results in a striking enhancement in glyphosate degradation rates, surpassing those of pristine $BiVO_4$ by two orders of magnitude. Furthermore, the optimized $BiVO_4$ was assembled on cellulose fabric and shows effective degradation capability in glyphosate-polluted soil. This study underscores the significance of rationally designing semiconductor photocatalysts at the nano-/micrometer scale for application in the removal of persistent environmental contaminants.

Received 12th September 2025,
Accepted 13th November 2025

DOI: 10.1039/d5qi01894c

rsc.li/frontiers-inorganic

Introduction

Organophosphorus contaminants (OCs) have been emerging as one kind of universal pollutant due to their widespread presence in agricultural environments, of which glyphosate (GP) stands out as the most prevalently used organophosphorus pesticide renowned for its broad-spectrum applicability and effectiveness in the control of weeds.[1–3] However, the extensive utilization of GP leads to residues in water and the soil, resulting in a potentially serious risk to public health and the ecological environment.[4] Currently, various treatment techniques, including adsorption, chemical oxidation, biodegradation, and photo-degradation, are employed to remove GP.[5–12] However, these methods possess some disadvantages, including a low capacity to capture GP, high energy consumption or the requirement of oxidants such as persulfates.[13–16]

Photocatalysis is emerging as a promising approach for environmental remediation owing to its various merits, including complete mineralization, no secondary pollution, low cost, and mild operating temperature and pressure conditions.[17–19] Photogenerated charge separation is a key process that determines the efficiency of semiconductor-based photocatalysis.[20–23] Charge separation among different facets of photocatalysts has gained more attention for its feasibility in promoting charge separation and the rational assembly of cocatalysts on particulate photocatalysts.[24,25] Meanwhile, the decoration of cocatalysts or an interfacial layer is a universal strategy for optimizing photocatalytic reaction.[26,27] Facet engineering has also been shown to activate the contaminant molecules due to the unique surface structure.[28–30] In particular, $BiVO_4$ is one of the most representative photocatalysts with the definite spatial separation of photogenerated electrons and holes among the {010} and {110} facets.[31] The ideal behavior of the charge carriers is driven by the variance of the surface energy among different facets that function as facet heterojunctions. The distinct spatial separation of charge carriers is favorable to the regulation of specific reactions for the particular reaction sites on different facets. Furthermore, it was reported that selective decoration of cocatalysts on specific crystal facets of semiconductors could modify the reaction

[a]*State Key Laboratory of Tea Plant Germplasm Innovation and Resource Utilization, Agricultural Photocatalysis Laboratory, School of Materials and Chemistry, Anhui Agricultural University, Hefei 230036, China*
[b]*State Key Laboratory of Catalysis, Dalian National Laboratory for Clean Energy, Dalian Institute of Chemical Physics, Chinese Academy of Sciences, Dalian 116023, P. R. China*
†These authors contributed equally to this work.

path due to the uniform electronic and structural properties.[25,32] One of the key challenges is how to accomplish the high generation rate of reactive oxygen species (ROS), which are the crucial species acting as oxidizing reagents for degradation, and the formation mechanism of ROS involves the participation of photogenerated electrons or holes.[33–35] Nevertheless, how the crystal facets of semiconductor-based photocatalysts affect the formation of ROS is still elusive. Moreover, unraveling the role of cocatalysts in oxidized degradation reactions on particulate photocatalysts is crucial for the efficient removal of persistent organic contaminants from polluted water and soil.

Herein, we report the photocatalytic removal of glyphosate using a decahedron $BiVO_4$ photocatalyst with the rational assembly of Pd and MnO_x cocatalysts spatially on different facets. Facet-selective deposition of Pd nanoparticles as a cocatalyst onto the {010} facets results in a remarkable promotion of charge separation and acceleration of the oxygen reduction reaction, leading to the generation of $^{\bullet}O_2^-$ radicals, which serve as the main reactive species for glyphosate degradation. Further construction of MnO_x on the hole-accumulating {110} facets facilitates the water oxidation reaction to promote the production of $^{\bullet}OH$ radicals. The synergistic integration of the Pd and MnO_x dual cocatalysts gives a remarkable augmentation of the glyphosate degradation rates compared to $BiVO_4$. Cellulose non-woven fabric is an eco-friendly material derived from natural cellulose fibers, renowned for its biodegradability, lightweight, and excellent hydrophilic properties,[36] making it an ideal support for the $BiVO_4$ photocatalyst in wastewater treatment. Moreover, the optimized $BiVO_4$-coated cellulose fabric can be implemented in flow panel systems for agricultural contaminant degradation in tea plantation soil, and exhibits superior activity for glyphosate with an average removal rate over 80%. This universal strategy holds great significance in addressing pesticide pollution and advancing the goal of green agriculture.

Experimental

Chemicals

Glyphosate (Innochem, 95%), $Bi(NO_3)_3{\cdot}5H_2O$ (Sinopharm Chemical, AR), NH_4VO_3 (Sinopharm Chemical, AR), $NH_3{\cdot}H_2O$ (Sinopharm Chemical, AR), $PdCl_2$ (Sinopharm Chemical, 99.9%), $AgNO_3$ (Sinopharm Chemical, 99.8%), H_2PtCl_6 (Sinopharm Chemical, AR), $Ni(NO_3)_2{\cdot}6H_2O$ (Sinopharm Chemical, AR, 98%), $Co(NO_3)_2{\cdot}6H_2O$ (Sinopharm Chemical, AR, 98.5%), $MnSO_4$ (Sinopharm Chemical, AR, 98%), dihydroethidium (DHE, Yeasen, ≥90%), nitrotetrazolium blue chloride (NTB, Macklin, 98%), and 3,3′,5,5′-tetramethylbenzidine (TMB, Macklin, 99%) were used. All reagents were used as received without further purification.

Synthesis of decahedron $BiVO_4$ crystals

Decahedron $BiVO_4$ crystals were synthesized as previously reported.[31] Typically, the precursors NH_4VO_3 (36 mmol) and $Bi(NO_3)_3{\cdot}5H_2O$ (36 mmol) were dissolved in 300 mL of 2.0 M nitric acid solution, and the pH value of the solution was then adjusted to 2.0 with ammonia solution under stirring until the formation of an orange precipitate. After about 2 h of aging, the orange precipitate at the bottom of the beaker was transferred to a Teflon-lined stainless-steel autoclave with a capacity of 100 mL and hydrothermally treated at 200 °C for 24 h. After the autoclave was cooled to room temperature, a vivid yellow powder was separated by filtration, washed with deionized water more than 3 times, and then dried at 60 °C in air overnight.

Facet-selective photo-deposition of metals and/or oxides

Three different deposition routes (single photo-reduction, single photo-oxidation and simultaneous photo-reduction and photo-oxidation) were adopted, and all the photo-depositions were similarly carried out at room temperature without adjusting the pH value. Typically, 0.50 g of $BiVO_4$ powder and a calculated amount of deposition precursor (1 wt% noble metal or 0.5 wt% metal oxide) were mixed in 100 mL of deionized water, and the suspension was then irradiated by a 300 W Xe lamp ($\lambda \geq 420$ nm) under continuous stirring. After 5 h photodeposition, the suspension was filtered, washed with deionized water more than 3 times, and finally dried at 60 °C overnight. The as-obtained powder was used for characterizations and/or activity tests. As for the photo-reduction of the single Au, Pd or Ag particles, $HAuCl_4$, $PdCl_2$ and $AgNO_3$ were chosen as precursors, respectively, and the as-synthesized samples were denoted as Au (Pd, or Ag)/$BiVO_4$, respectively. To ensure the counterpart oxidation reaction, 20% methanol as a hole scavenger was also used as a sacrificial reagent for comparison. The photo-oxidation of the single MnO_x, CoO_x or NiO_x was achieved with $MnSO_4$, $Co(NO_3)_2$ or $Ni(NO_3)_2$ as a precursor, and $NaIO_3$ was employed as the electron acceptor. The as-prepared samples were denoted as $MnO_x/BiVO_4$, $CoO_x/BiVO_4$ and $NiO_x/BiVO_4$, respectively. For $Pd/MnO_x/BiVO_4$, the deposition process is the same as that of $MnO_x/BiVO_4$ except for the replacement of $BiVO_4$ with $Pd/BiVO_4$. For the impregnated sample, MnO_x was impregnated from $MnSO_4$ solution by post-calcination at 350 °C for 1 h, and the as-prepared sample was denoted as MnO_x(imp)/$BiVO_4$.

Characterization

The as-prepared $BiVO_4$ samples were characterized using X-ray powder diffraction (XRD) on a Rigaku SmartLab powder diffractometer. The scan rate of 20° min^{-1} was applied to record the XRD patterns in the range of 10–60° at a step size of 0.01°. UV–visible (UV–vis) diffuse reflectance spectra were recorded on a UV–vis spectrophotometer (UV-2600, Shimadzu) equipped with an integrating sphere. The morphologies and particle sizes were examined by scanning electron microscopy (SEM, S4800, Hitachi) and high-resolution scanning electron microscopy (HRSEM, S5500, HITACHI).

Photocatalytic degradation experiments

The photocatalytic degradation performance of the $BiVO_4$ system was evaluated in an in-house-fabricated photoreactor

(250 mL) using a 300 W Xe lamp (Beijing Perfectlight Technology Co., Ltd). Normally, 20 mg photocatalyst was dispersed in the 20 ppm glyphosate solution and stirred in the dark for 2 h, followed by visible light irradiation (λ >420 nm). After different times, 5 mL suspensions were taken out and extracted using a 0.22 μm membrane filter for later detection. The concentration of glyphosate was detected by high-performance liquid chromatography (HPLC system, Agilent 1260). An Agilent C18 column (250 × 4.6 mm, 5 μm) with the mobile phases of 20 mM PBS (A: 90%) and methanol (B: 10%) and a flow rate of 1.0 mL min^{-1} was employed.

Preparation of the Pd/MnO_x/$BiVO_4$-loaded Cellulose fabric

500 mg of Pd/MnO_x/$BiVO_4$ powder was dispersed in 100 mL of 0.5 wt% Nafion isopropanol and ultrasonicated for 2 minutes to obtain a homogeneous suspension. The homogeneous suspension was dropped onto the cellulose-based non-woven fabric (25 cm × 25 cm), and the non-woven fabric was dried in a fume hood for 1 h to evaporate the solvent. Finally, the Pd/MnO_x/$BiVO_4$-loaded fabric was washed in deionized water to remove the loosely adhered Pd/MnO_x/$BiVO_4$.

Results and discussion

The decahedron $BiVO_4$ photocatalyst was synthesized using a previously reported hydrothermal process.[31] The as-prepared $BiVO_4$ shows a smooth surface with a regular decahedron morphology and a size of 1–2 μm, and the crystal structure is in accordance with the pure monoclinic scheelite phase (Fig. S1–S4). Meanwhile, the crystallite size is calculated to be 430 nm according to the corresponding XRD peak of the (010) crystallographic plane. As depicted in Fig. 1a, the deposition of the cocatalyst was carried out using an *in situ* photo-deposition method (the sample is denoted as X/$BiVO_4$, X= Au, Ag, Pd, CoO_x, NiO_x, MnO_x). It can be clearly observed that selectively reduced deposition of metallic nanoparticles (Au, Ag, Pd) occurs on the (010) facet of the $BiVO_4$ decahedron particles, while photo-oxidation of metal ions to metal oxide species (CoO_x, NiO_x, MnO_x) only occurs on the (110) facets (Fig. S5 and S6). These results indicate that spatial charge separation and selective photo-deposition between the (010) and (110) facets can be well maintained in our prepared $BiVO_4$ crystals. Thereafter, dual cocatalysts (Pd and MnO_x) were sequentially deposited as cocatalysts on specific facets. The SEM images show the morphology of the dual cocatalyst-deposited $BiVO_4$, where it can be seen that the oxidation and reduction cocatalysts are successfully deposited on the (110) and (010) facets of $BiVO_4$, respectively (Fig. 1b and S7). The deposited Pd nanoparticles are highly dispersed on the (010) facet with a size of 2–10 nm, and the particle density is about 8000 per μm^2 (Fig. S8). Their existence is further confirmed by high-resolution TEM (Fig. 1c and d), in which the planar spacing of 0.22 nm well matches the (111) plane of metallic Pd.[37] The oxidation cocatalyst MnO_x can also be validated on the hole-rich (110) facets of $BiVO_4$, as shown by the TEM and HRTEM images (Fig. 1e and f) and the elemental mapping (Fig. 1g and S8).[38] The optical properties remain invariable for the samples with cocatalyst deposition (Fig. S9). Furthermore, EDX imaging for the different facets of Pd/MnO_x/$BiVO_4$ also shows that the different substances on the different facets represent MnO_x and Pd, respectively (Fig. 1g).

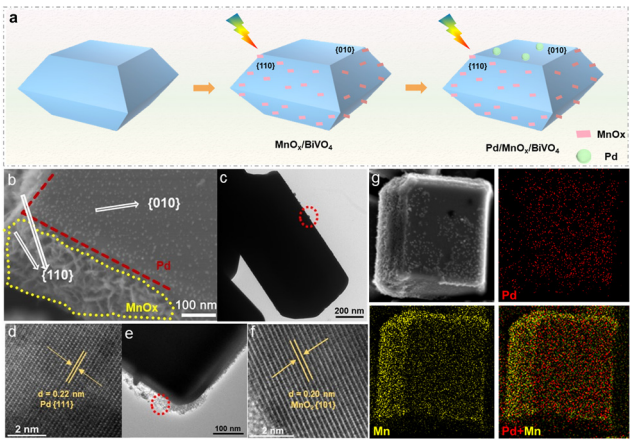

Fig. 1 Morphology characterization of the $BiVO_4$ photocatalysts. (a) Schematic illustration for the photo-deposition. (b) SEM image of Pd/MnO_x/$BiVO_4$. (c) TEM image of Pd on Pd/MnO_x/$BiVO_4$, and (d) HRTEM image of metal Pd in c. (e) TEM image of MnO_x on Pd/MnO_x/$BiVO_4$, and (f) HRTEM image of MnO_x in e. (g) Element mapping images of Pd/MnO_x/$BiVO_4$.

Thermogravimetric analysis (TGA) of MnO_x/$BiVO_4$ and Pd/MnO_x/$BiVO_4$ exhibits high thermal stability with negligible weight loss step at 25–500 °C (Fig. S10). Pd/MnO_x/$BiVO_4$ shows an increase in surface area (5.77 m^2 g^{-1}) *versus* MnO_x/$BiVO_4$ (4.03 m^2 g^{-1}) by BET measurement, confirming enhanced active site exposure for the highly dispersed Pd cocatalyst (Fig. S11).

The photocatalytic degradation performance of glyphosate by $BiVO_4$ photocatalysts with different reduction cocatalysts was evaluated first. As observed in Fig. 2a, the bare $BiVO_4$ with a simple crystal facet effect just presents poor activity for photocatalytic decomposition of glyphosate, indicating that the pristine decahedron $BiVO_4$ is unable to accomplish the effective degradation of glyphosate. On implementing the selective deposition of Ag nanoparticles, the degradation activity of Ag/$BiVO_4$ exhibits a negligible increase, and superior performance is realized when the Ag is replaced by Au, with the degradation efficiency of 50% in 250 min. While the glyphosate degradation is significantly promoted by Pd cocatalyst-decorated $BiVO_4$, the efficiency distinctly increases to 80% within 120 min. The kinetic constant is also significantly enhanced with metal cocatalyst deposition, especially for the Pd cocatalyst (Fig. 2b). As noble metals with a relatively large work function on $BiVO_4$ promote the electron transfer from $BiVO_4$ to metal nanoparticles, the decoration of Pd could enhance charge separation. The choice of suitable reduction cocatalysts is substantial for constructing efficient photocatalytic degradation systems of glyphosate. As Pd is generally

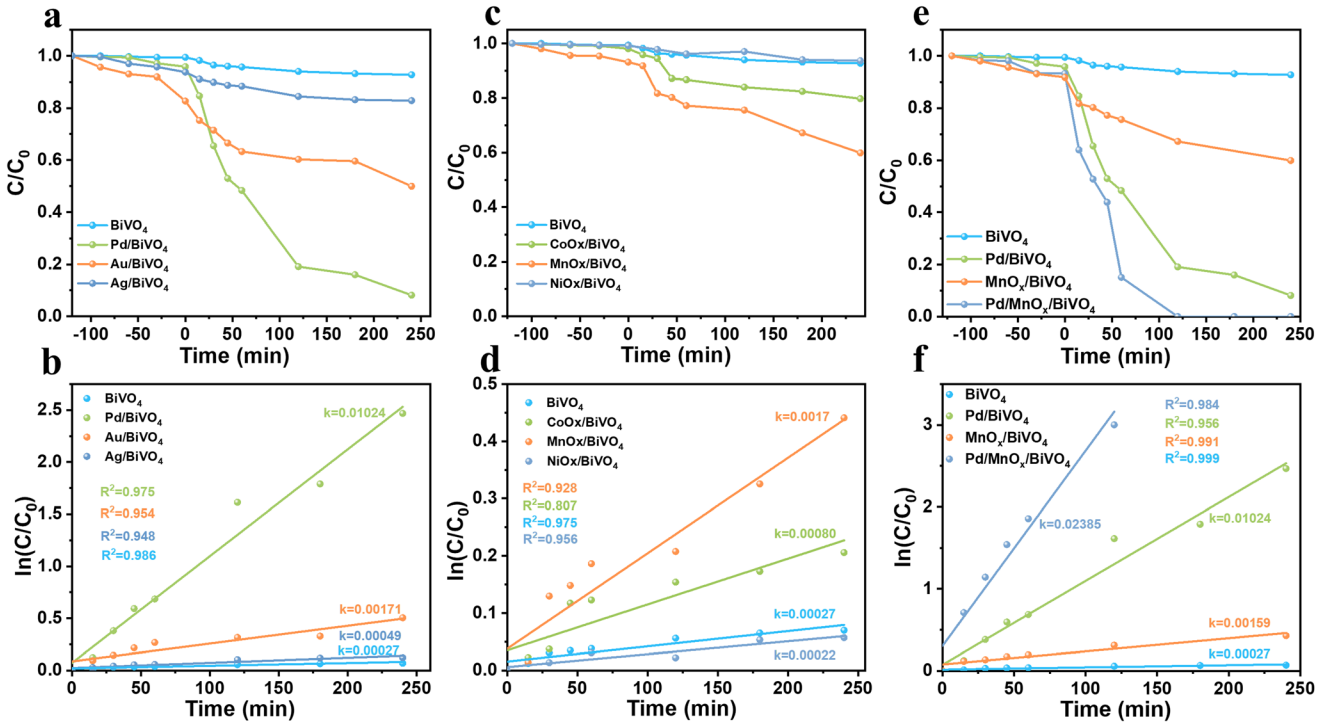

Fig. 2 (a) Photocatalytic degradation performance of the M/$BiVO_4$, where M represents Au, Ag, or Pd. (b) Kinetic analysis of glyphosate degradation processes by M/$BiVO_4$. (c) Photocatalytic degradation performance of the MO_x/$BiVO_4$, where MO_x represents CoO_x, NiO_x, or MnO_x. (d) Kinetic analysis of glyphosate degradation processes by MO_x/$BiVO_4$. (e) Photocatalytic degradation curves of glyphosate by $BiVO_4$, Pd/$BiVO_4$, MnO_x/$BiVO_4$, and Pd/MnO_x/$BiVO_4$. (f) Degradation kinetics curves of the corresponding $BiVO_4$ samples. Reaction conditions: 20 ppm glyphosate, 100 mL solution, 50 mg photocatalyst, λ >420 nm.

utilized in O_2 reduction reactions as a cocatalyst due to its excellent performance, the enhanced mechanism is very likely the result of O_2 reduction to produce a sufficient amount of $^{\bullet}O_2^-$, thus leading to fast glyphosate degradation through a free radical-related reaction process.

Correspondingly, different oxidation cocatalysts were also employed in $BiVO_4$, and Fig. 2c shows the photocatalytic degradation performance of different metal oxides (MnO_x, CoO_x, and NiO_x) as oxidation cocatalysts. It can be seen that the loading of the single oxidation cocatalyst can only achieve slightly better activities for the photocatalytic degradation of glyphosate, and better performances were all obtained for different oxide cocatalyst-loaded $BiVO_4$ than bare $BiVO_4$. The activity order is MnO_x > CoO_x > NiO_x, which is more evident as indicated by the degradation kinetics (Fig. 2d). The results indicate that the mere loading of MnO_x on $BiVO_4$ can lead to relatively low enhancement of photocatalytic degradation. Specifically, when only Pd was deposited as the cocatalyst, the degradation activity of glyphosate was increased much more obviously than that with only MnO_x as the cocatalyst. It seems that the reduction reaction (generating $^{\bullet}O_2^-$) is the possible rate-determining step for the degradation of glyphosate. However, when only the reduction cocatalyst was deposited on $BiVO_4$, the reaction activity was still unsatisfactory.

In this case, the dual cocatalysts were selectively decorated on $BiVO_4$ subsequently. Naturally, the degradation performance of glyphosate in the dual cocatalyst system (Pd/MnO_x/$BiVO_4$) is obviously superior to that of the single cocatalyst system (Fig. 2e). The possible reason is that dual cocatalysts substantially facilitate the extraction of photogenerated carriers owing to the selective deposition on specific facets appropriately, and the proper location of the Pd cocatalyst subsequently provides abundant active sites for O_2 reduction to $^{\bullet}O_2^-$. Meanwhile, the dual cocatalysts have a synergistic effect on charge separation, thus resulting in distinguished degradation for glyphosate. The degradation curve obeys the pseudo-first-order kinetic equation, and the rate constant is determined to be 0.024 min^{-1} for Pd/MnO_x/$BiVO_4$, which is 2.4 times higher than that of Pd/$BiVO_4$ (0.010 min^{-1}), while the degradation constants by sole $BiVO_4$ and MnO_x/$BiVO_4$ are very slow (Fig. 2f). The evident synergetic effect of dual cocatalysts is amply validated by comparison of $BiVO_4$ with a single cocatalyst or dual cocatalysts selectively deposited on the corresponding correct facets. Furthermore, these results indicate that the Pd cocatalyst is particularly vital for the removal of glyphosate and verify the importance of the simultaneous deposition of dual cocatalysts. Moreover, the stability tests over 3 cycles indicate satisfactory stability of Pd/MnO_x/$BiVO_4$ (Fig. S12). The XRD and SEM analyses indicated that the morphology and crystalline structure remained well after the stability test (Fig. S13 and S14). The ICP analysis of the post-reaction solution demonstrated that the dissolution of the

cocatalysts is negligible (Table S1). These results highlight the stability of the Pd/MnO_x/$BiVO_4$ photocatalyst after multiple reaction cycles.

The valence states of MnO_x/$BiVO_4$ and Pd/MnO_x/$BiVO_4$ were examined using X-ray photoelectron spectroscopy (XPS). The XPS results confirm the Mn^{3+} and Mn^{4+} oxidation state for both MnO_x/$BiVO_4$ and Pd/MnO_x/$BiVO_4$, which is consistent with the previous literature[39] (Fig. S15, S16 and Tables S2, S3). The binding energy of Pd 4f reveals that the deposited Pd element on the $BiVO_4$ exists in metallic form for the Pd/$BiVO_4$ sample (Fig. S16 and Table S3). The valence state of the deposited Pd, including the positive chemical state of Pd^{2+}, may result from self-oxidation of metallic Pd on exposure to air.[40] The states of Pd/MnO_x/$BiVO_4$ were also explored after the stability test, and the XPS results indicate partial oxidation of MnO_x species as the role of the oxidation cocatalyst, while the states of Pd are nearly the same as those of the prepared Pd/MnO_x/$BiVO_4$ (Fig. S16 and Tables S3, S4).

The electrochemical performance of O_2 reduction was explored in O_2-saturated electrolyte solution for the above $BiVO_4$ samples with different noble metals (Au, Ag, Pd). The current density curves all exhibit the typical characteristic of O_2 reduction for the three metals (Fig. 3a).[41] Notably, the performance is remarkably increased for Pd/$BiVO_4$ as compared with the others, indicating the excellent activity of Pd nanoparticles in the oxygen reduction reaction. Mott–Schottky analysis quantitatively determines the conduction band (CB) edge of $BiVO_4$ at 0.05 V *vs.* RHE (Fig. S17a), and thus the valence band (VB) is established at 2.45 V *vs.* RHE according to the bandgap of 2.4 eV derived from UV–vis absorption.[42] The valence band edge of $BiVO_4$ (2.45 V *vs.* RHE) exceeds the $^{\bullet}OH$/H_2O potential (2.31 V *vs.* RHE), and thus is favorable to produce $^{\bullet}OH$.[43] The band alignment diagrams for various $BiVO_4$ samples show negligible variance, which indicates the nearly invariable energy band structure (Fig. S17b). Moreover, the *in situ* EPR signals using DMPO as a probe molecule of $^{\bullet}OH$ demonstrate that MnO_x/$BiVO_4$ exhibits substantial intensity compared to $BiVO_4$, indicating that the MnO_x can promote the generation of $^{\bullet}OH$ (Fig. S18). Photoelectrochemical measurement was also conducted on $BiVO_4$ and MnO_x/$BiVO_4$, as only the oxidation half-reaction is evaluated, and the charge extraction driving force provided by the loaded Pd is relatively weak compared to the applied bias. The results verified the significance of selective deposition of MnO_x on $BiVO_4$, as the photocurrent response of MnO_x/$BiVO_4$ is superior to the impregnated sample MnO_x(imp)/$BiVO_4$ (Fig. S19).

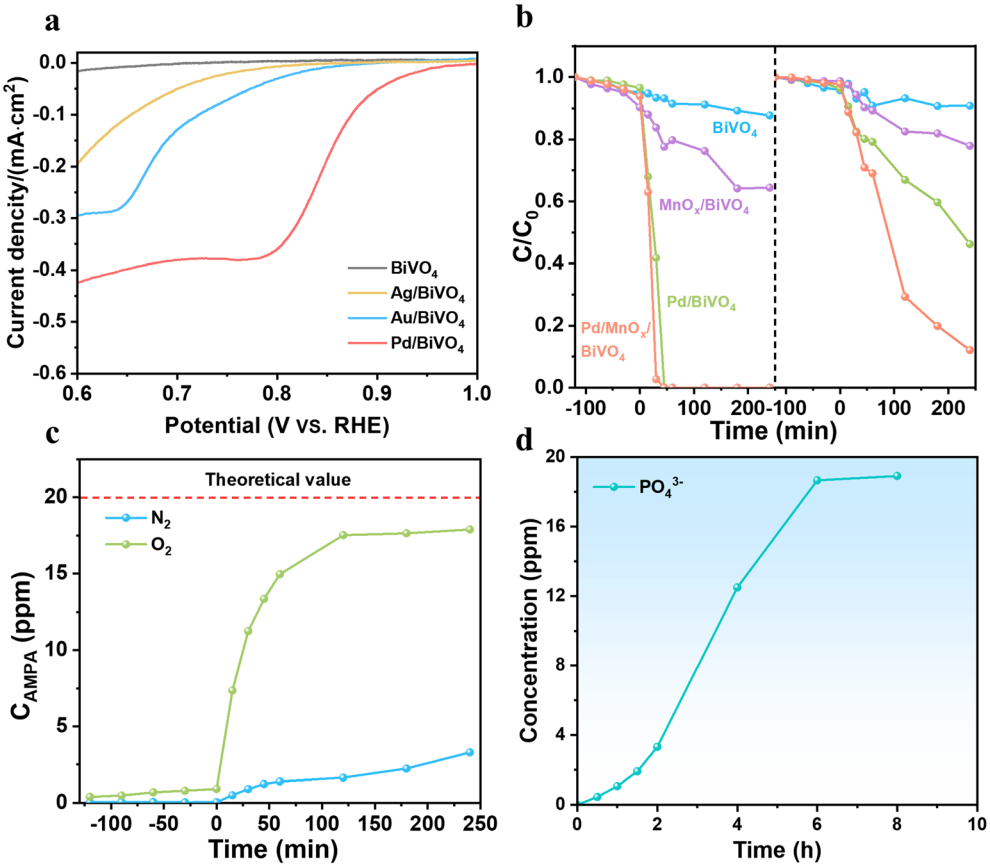

Fig. 3 (a) Electrochemical O_2 reduction curves for Ag, Au and Pd deposited on $BiVO_4$ in O_2-saturated electrolyte solution (0.5 M Na_2SO_4). (b) Photocatalytic degradation curves of glyphosate by different $BiVO_4$ samples in a continuous gas stream (O_2 or N_2). (c) The corresponding production on the Pd/MnO_x/$BiVO_4$ photocatalyst under an N_2 or O_2 atmosphere. (d) The concentration of mineralized PO_4^{3-} in the degradation period of 8 h.

Photoelectrochemical impedance spectroscopy (PEIS) of Pd/MnO_x/$BiVO_4$ exhibits an evidently smaller charge-transfer resistance compared to pristine $BiVO_4$, Pd/$BiVO_4$ and MnO_x/$BiVO_4$, confirming accelerated charge separation (Fig. S20a). Furthermore, the decay of photoluminescence (PL) of Pd/MnO_x/$BiVO_4$ shows a prolonged carrier lifetime (τ = 13.5 ns *vs.* 5.2 ns for $BiVO_4$ and the others), indicating suppressed electron–hole recombination due to dual cocatalyst-induced separation (Fig. S20b). When the MnO_x cocatalyst was randomly deposited on the (110) facets, the photocurrent was obviously increased as compared with the bare $BiVO_4$ electrode. This demonstrates that the photocurrent can be efficiently promoted even when the oxidation cocatalyst is randomly distributed on the $BiVO_4$. In addition, the increased photocurrent of Pd/MnO_x/$BiVO_4$ is 3 times higher than that of the $BiVO_4$ electrode with MnO_x randomly deposited on all of the facets. This indicates that the MnO_x can function efficiently for synchronously accelerating charge separation and surface reaction, which is in good agreement with the results of photocatalytic degradation experiments.

The role of O_2 was examined to identify the determining factor during glyphosate degradation. As shown in Fig. 3b, the degradation efficiency is further increased for all of the $BiVO_4$ samples as the glyphosate degradation proceeds in streaming pure O_2 conditions, and complete degradation is accomplished within 60 min for Pd/MnO_x/$BiVO_4$. The corresponding pseudo-first-order rate constants (k_{obs}) are calculated to be 0.05 min^{-1}, demonstrating that the degradation process of glyphosate is mainly accompanied by O_2 participation (Fig. S21a). Furthermore, from another control experiment in N_2 streaming, the results show that the degradation efficiency of glyphosate in an anaerobic system is only 70% within 120 min, and the degradation rate constants decrease to 0.0092 min^{-1} (Fig. 3b and Fig. S21b). Obviously, O_2 reduction to $^{\bullet}O_2^-$ plays a pivotal role in the aerobic system, while the decomposition of glyphosate in anaerobic conditions is severely hindered due to the lack of $^{\bullet}O_2^-$. The degradation is hindered because the generation of $^{\bullet}O_2^-$ is forbidden under anaerobic conditions, implying that O_2 is essential for glyphosate degradation by the $BiVO_4$ system. Furthermore, the appropriate accumulation of photogenerated electrons on the (010) facet is of great benefit to the subsequent O_2 reduction on Pd nanoparticles, which is reasonable to maximize the synergistic effect of spatial charge separation on specific facets and the rational construction of reactive sites for rapid production of $^{\bullet}O_2^-$ with adequate O_2 supply. The blank experiment was conducted to examine the possible mechanism of direct reduction of p-benzoquinone to hydroquinone by excited electrons,[44] and the results showed negligible production of hydroquinone in the ultraviolet absorption spectra (Fig. S22). The argon-degassed system exhibits significant attenuation of glyphosate degradation by 78% (Fig. S23), while O_2-saturated solutions evidently enhanced the degradation efficiency. These experiments conclusively validate the photocatalytic role of $^{\bullet}O_2^-$ and exclude the BQ/HQ side reaction.

Interestingly, the degradation products under O_2 obtained by liquid chromatography–mass spectrometry (LCMS) indicated that Pd/MnO_x/$BiVO_4$ selectively decomposes glyphosate to aminomethylphosphonic acid (AMPA), and the formation of AMPA is well in agreement with the removal of glyphosate (Fig. 3c). To evaluate the toxicity of the degradation products, we further monitored the concentration of PO_4^{3-} over a long period of 8 h as organophosphate derivatives are the main toxic substances (Fig. 3d). The combined results of AMPA and PO_4^{3-} indicates that glyphosate decomposes to AMPA initially (within 2 h), and then the AMPA is further cleaved, releasing PO_4^{3-} anions as the degradation of glyphosate is completed.

To verify the primary active spices responsible for glyphosate degradation by $BiVO_4$, we employed benzoquinone (BQ), methanol (CH_3OH), isopropyl alcohol (IPA), and potassium dichromate ($K_2Cr_2O_7$) to trap $^{\bullet}O_2^-$, h^+, $^{\bullet}OH$, and e^-, respectively (Fig. S24). To prominently distinguish the performance differences in capturing different radicals, we normalized the degradation efficiency against a normal control sample in Fig. 4. As shown in Fig. 4a, the normalized degradation efficiencies of glyphosate exhibit irregularity for bare $BiVO_4$ upon adding any scavengers due to the sluggish degradation kinetics. The performances are both enhanced upon adding CH_3OH and IPA for Pd/$BiVO_4$, which results from the inhibited photoexcited carrier recombination due to the rapid consumption of h^+ and $^{\bullet}OH$ by CH_3OH and IPA, allowing more photo-

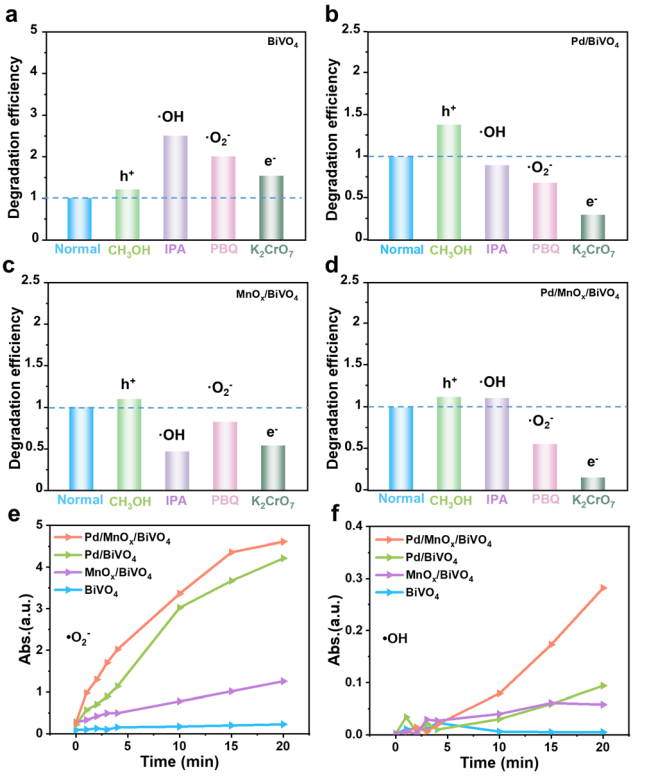

Fig. 4 Normalized degradation efficiencies of glyphosate with the addition of various scavengers by (a) $BiVO_4$, (b) Pd/$BiVO_4$, (c) MnO_x/$BiVO_4$, and (d) Pd/MnO_x/$BiVO_4$. Time dependence of light absorption for ROS generation under irradiation. (e) $^{\bullet}O_2^-$ production by NBT as a detector probe. (f) $^{\bullet}OH$ production by TMB as a detector probe.

generated electrons to migrate to the Pd surface for $^{\bullet}O_2^-$ generation. However, after adding BQ, the degradation rate by Pd/$BiVO_4$ decreased significantly, suggesting that $^{\bullet}O_2^-$ is dominant in the glyphosate degradation reaction. The capture result of $K_2Cr_2O_7$ further demonstrates the role of $^{\bullet}O_2^-$ as the degradation activity decreases faster *via* the impediment of O_2 reduction (Fig. 4b). As for MnO_x/$BiVO_4$, the photocatalytic degradation performance is slightly promoted with the addition of CH_3OH (Fig. 4c). Meanwhile, the degradation activity of the MnO_x/$BiVO_4$ system decreases when IPA and $K_2Cr_2O_7$ are added as scavengers for $^{\bullet}OH$ and e^-. This results from the fact that the MnO_x is responsible for accelerating charge separation, and that the main active radicals are $^{\bullet}OH$ and e^--induced $^{\bullet}O_2^-$. Additionally, we found a similar tendency for the photocatalytic activity of the Pd/MnO_x/$BiVO_4$ system with Pd/$BiVO_4$ after adding different scavengers (Fig. 4d). This indicates that $^{\bullet}O_2^-$ radicals play a dominant role in the photocatalytic degradation of glyphosate by Pd/MnO_x/$BiVO_4$.

The production of ROS was semi-quantitatively measured by visible light absorption spectroscopy. The nitroblue tetrazolium (NBT) was used as a probe molecule to measure the production of $^{\bullet}O_2^-$.[45] The increased absorption intensity of NBT also suggests the increase of $^{\bullet}O_2^-$ with continuous irradiation, as shown in Fig. 4e. The yield of $^{\bullet}O_2^-$ on dual cocatalyst-decorated $BiVO_4$ rises dramatically compared to the one produced by single cocatalyst-decorated $BiVO_4$ and is six times higher than that of bare $BiVO_4$, suggesting that the combination of $BiVO_4$ and cocatalysts enhanced the yield of $^{\bullet}O_2^-$. The production of $^{\bullet}OH$ could be measured by 3,3′,5,5′-tetramethylbenzidine (TMB).[46] A slight enhancement in absorption intensity is observed for all of the samples, indicating that photo-induced production of $^{\bullet}OH$ is more favorable after the deposition of MnO_x (Fig. 4f). These results suggest that both $^{\bullet}O_2^-$ and $^{\bullet}OH$ radicals are promoted on the Pd/MnO_x/$BiVO_4$ photocatalyst under visible light, which is responsible for the greatly enhanced photocatalytic degradation rates. Comparative analysis with published photocatalytic glyphosate degradation studies demonstrates that our system achieves predominant degradation performance with nearly complete efficiency within 120 min and further mineralization of organophosphorus (Table S5). Moreover, our work reveals that the selective decoration of dual cocatalysts on facet-engineered $BiVO_4$ can strengthen the generation of specific radicals, which highlights the significant scientific merit and potential applications in the degradation of other pollutants and selectivity regulation.

To further map the crystal facet-dependent photocatalytic reaction sites of O_2 reduction, laser scanning confocal fluorescence microscopy (LSCM) was used to investigate the population of $^{\bullet}O_2^-$ on individual $BiVO_4$ particles (Fig. 5a). The dihydroethidium (DHE) oxidation induced by $^{\bullet}O_2^-$ is taken as the probe reaction, which produces fluorescence at 610 nm.[47] Fluorescence mapping for the $BiVO_4$ crystals was implemented in an air-saturated solution containing fluorescent probe molecules under a 488 nm laser. As shown in Fig. 5b, evident green fluorescence was observed during irradiation, and the locations entirely overlapped on the surface of the $BiVO_4$ crystals. The fluorescence signal can be ascribed to the intrinsic photoluminescence of excited $BiVO_4$.[48] Moreover, the fluorescence magnitude of the oxidized probe molecules is too faint to be detected, suggesting that electron-induced oxygen reduction nearly does not occur on the bare $BiVO_4$ (Fig. 5c and d). A similar appearance of intrinsic photoluminescence is also observed on dual cocatalyst-decorated $BiVO_4$ (Fig. 5e and f). Interestingly, the bright red fluorescence clearly indicates

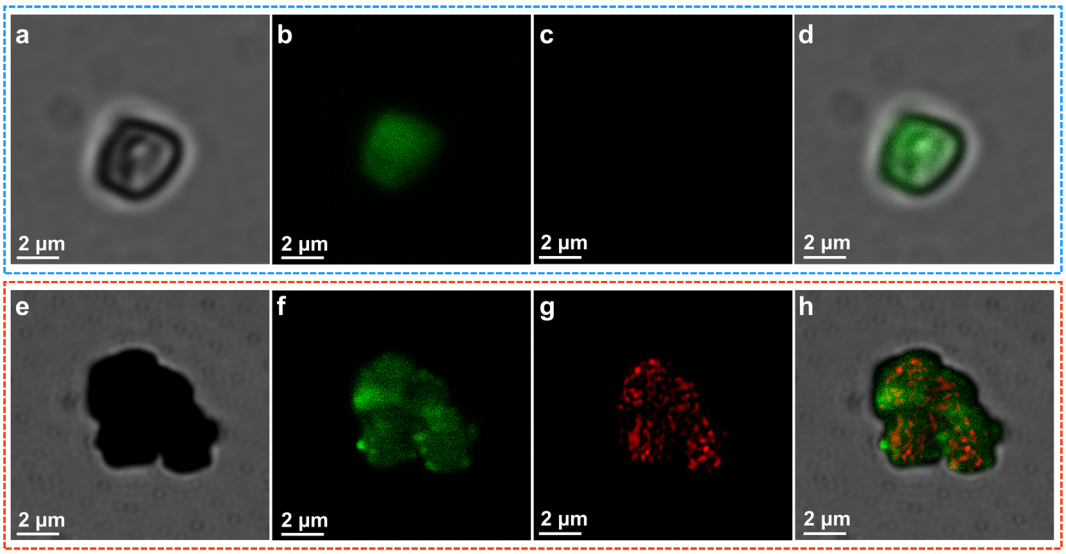

Fig. 5 Laser scanning confocal fluorescence microscopy of $BiVO_4$ (a–d) and Pd/MnO_x/$BiVO_4$ (e–h). (a) Bright field image, (b) fluorescence mapping at 535 nm, (c) fluorescence mapping at 613 nm and (d) the overlapping image of $BiVO_4$; (e) bright field image, (f) fluorescence mapping at 535 nm, (g) fluorescence mapping at 613 nm and (h) the overlapping image of Pd/MnO_x/$BiVO_4$.

strong enhancement on the generation of O_2^- for Pd/MnO_x/$BiVO_4$, indicating that the activity of electron-induced O_2 reduction is dominated synergistically by charge separation and catalytic processes (Fig. 5g). Surprisingly, red fluorescence spots of the DHE probe on the green background were found to be remarkable and preferentially located on the lateral (010) facet of the $BiVO_4$ decahedrons due to the selective deposition of Pd nanoparticles on the (010) facet (Fig. 5h). The above results validate that the reaction of photocatalytic O_2 reduction to $^{\bullet}O_2^-$ is related to the accumulation of photogenerated electrons and Pd cocatalyst decoration simultaneously, which results from the spatial charge separation and related reduction reaction. In addition to the photogenerated holes and electrons preferentially distributing at the different facets of the $BiVO_4$ microcrystal photocatalysts, we further reveal that the reduction of O_2 tends to occur at the Pd sites on the (010) facet.

As glyphosate is one kind of common pesticide residue in agricultural soil, the photocatalytic degradation of glyphosate in soil was conducted by Pd/MnO_x/$BiVO_4$. As the traditional configuration that combines a slurry of photocatalyst powder and soil dispersion is unpractical as soil is an effective shield against light, we assembled a continuous flow reactor to examine the photocatalytic degradation capability for polluted soil remediation (Fig. 6a). Thus, a separated configuration with two parallel individual chambers was developed to ensure the light absorption by the photocatalyst powder while keeping it separate from the soil sample. As presented in Fig. 6b, the reactor is composed of a water inlet system, a photocatalyst chamber, a soil chamber, a water outlet system, and a water circulation system. To ensure the light absorption efficiency, the upper chamber is covered by Pd/MnO_x/$BiVO_4$-loaded cellulose membrane for adequate light incidence, followed by the soil layer being placed in the bottom chamber. A continuous water stream flows from the photocatalyst chamber to the soil layer through the membrane, and thus, the eluted free glyphosate molecules from the soil can be taken to the photocatalyst chamber for degradation.

To validate the degradation practicability for polluted soil samples of our photocatalytic reactor, the degradation experiment was carried out under simulated solar irradiation. The degradation efficiency is up to 82% for the illumination time of 10 h. The average light intensity is about 60 mW cm^{-2}, which is fundamentally enough to guarantee the photocatalytic removal of glyphosate. The average removal efficiencies of glyphosate in soil were maintained above 70% after 5 cycles (Fig. 6c). The aforementioned results indicate that the glyphosate in soil can be effectively removed through consecutive flow by appropriately decorating the $BiVO_4$ system. Thus, the integrated photocatalytic degradation device based on dual cocatalyst $BiVO_4$ has promising prospects in soil recovery applications under natural conditions.

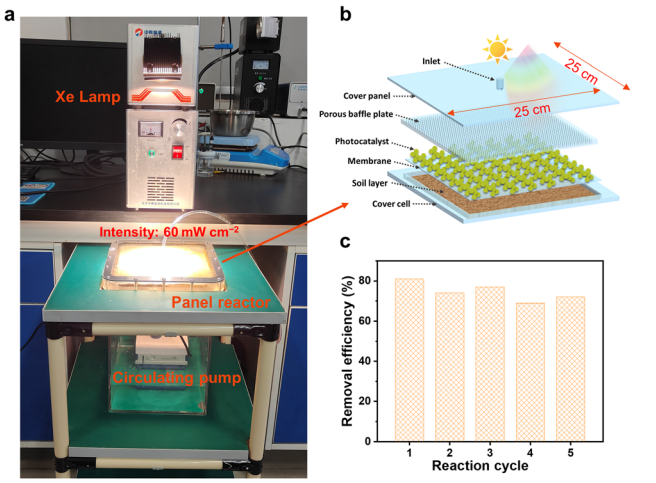

Fig. 6 Photocatalytic degradation of glyphosate for polluted soil in a cycle-flow reactor (effective size: 25 cm × 25 cm, glyphosate content: 5 ppm). (a) Photograph of the photocatalytic degradation of glyphosate by Pd/MnO_x/$BiVO_4$ in a continuous flow device. (b) Schematic diagram of the continuous-flow reactor structure. (c) Degradation efficiency of glyphosate for 5 cycles under simulated sunlight.

Conclusions

In summary, we successfully constructed a photocatalyst system with dual cocatalysts rationally decorated to achieve highly efficient degradation of glyphosate. Remarkably enhanced photocatalytic activities were observed for the rationally assembled photocatalysts. Systemic investigations show that the enhanced photocatalytic performances are ascribed to the intrinsic nature of spatial charge separation among different facets of $BiVO_4$ and the induced synergistic effect of dual cocatalyst selective deposition on specific facets of $BiVO_4$. This unique effect endows excellent performance for fast generation of $^{\bullet}O_2^-$ on selectively deposited Pd nanoparticles by accumulated photogenerated electrons. Concurrently, the construction of MnO_x on the hole-accumulating {110} facets promotes the water oxidation reaction, augmenting the production of $^{\bullet}OH$ radicals. These radicals serve as the primary reactive species responsible for the photocatalytic degradation of glyphosate. The synergistic integration of Pd and MnO_x dual cocatalysts onto different facets of $BiVO_4$ results in a striking enhancement of the glyphosate degradation rates, surpassing those of pristine $BiVO_4$ by two orders of magnitude. Furthermore, we assembled a Pd/MnO_x/$BiVO_4$-loaded cellulose fabric that shows effective remediation capability on glyphosate-polluted soil, suggesting potential in agricultural remediation. This work further demonstrates the distinctive property that spatial charge separation and selective deposition of dual cocatalysts on facet-engineered $BiVO_4$ can be expanded to the application of photocatalytic agricultural contaminant removal and other environmental remediation processes.

Author contributions

Nengcong Yang was responsible for conducting all the experiments, performing data analysis, and drafting the original

manuscript. Lulu Liu and Yue Chen performed the synthesis and characterization. Mengmeng Liu and Zhian Chen were involved in the experiments and data analysis. Ruyan Hou and Sheng Ye conducted a theoretical study. Rengui Li was responsible for review and editing. All the authors discussed the results and contributed to the writing of the paper.

Conflicts of interest

There are no conflicts to declare.

Data availability

The data supporting this article have been included as part of the supplementary information (SI). Supplementary information is available. See DOI: **https://doi.org/10.1039/d5qi01894c**.

Acknowledgements

This work was financially supported by the National Natural Science Foundation of China (NSFC, 22372001, 22502002), Starting Fund for Scientific Research of High-Level Talents, Anhui Agricultural University (rc382108), and Postdoctoral Fellowship Program of CPSF (GZB20240003). We thank Dr Qin Wang and Dr Yang Xu of the Biotechnology Center of Anhui Agricultural University for their help with material characterization in this work.

References

1 E. G. Jaworski, Mode of action of *N*-phosphonomethylglycine. Inhibition of aromatic amino acid biosynthsis, *J. Agric. Food Chem.*, 1972, **20**, 1195–1198.
2 T. Funke, H. Han, M. L. Healy-Fried, M. Fischer and E. Schönbrunn, Molecular basis for the herbicide resistance of Roundup Ready crops, *Proc. Natl. Acad. Sci. U. S. A.*, 2006, **103**, 13010–13015.
3 S. O. Duke, Taking stock of herbicide-resistant crops ten years after introduction, *Pest Manage. Sci.*, 2005, **61**, 211–218.
4 L. P. Agostini, R. S. Dettogni, R. S. dos Reis, E. Stur, E. V. W. dos Santos, D. P. Ventorim, F. M. Garcia, R. C. Cardoso, J. B. Graceli and I. D. Louro, Effects of glyphosate exposure on human health: Insights from epidemiological and in vitro studies, *Sci. Total Environ.*, 2020, **705**, 135808.
5 A. Pankajakshan, M. Sinha, A. A. Ojha and S. Mandal, Water-Stable Nanoscale Zirconium-Based Metal–Organic Frameworks for the Effective Removal of Glyphosate from Aqueous Media, *ACS Omega*, 2018, **3**, 7832–7839.
6 X. Zhu, B. Li, J. Yang, Y. Li, W. Zhao, J. Shi and J. Gu, Effective Adsorption and Enhanced Removal of Organophosphorus Pesticides from Aqueous Solution by Zr-Based MOFs of UiO-67, *ACS Appl. Mater. Interfaces*, 2015, **7**, 223–231.
7 M. Cycoń, A. Żmijowska, M. Wójcik and Z. Piotrowska-Seget, Biodegradation and bioremediation potential of diazinon-degrading Serratia marcescens to remove other organophosphorus pesticides from soils, *J. Environ. Manage.*, 2013, **117**, 7–16.
8 H. Hossaini, G. Moussavi and M. Farrokhi, The investigation of the LED-activated FeFNS-TiO_2 nanocatalyst for photocatalytic degradation and mineralization of organophosphate pesticides in water, *Water Res.*, 2014, **59**, 130–144.
9 N. Negishi, T. Sano, T. Hirakawa, F. Koiwa, C. Chawengkijwanich, N. Pimpha and G.-R. M. Echavia, Photocatalytic detoxification of aqueous organophosphorus by TiO_2 immobilized silica gel, *Appl. Catal., B*, 2012, **128**, 105–118.
10 H. Dong, Q. Xu, L. Lian, Y. Li, S. Wang, C. Li and X. Guan, Degradation of Organic Contaminants in the Fe(II)/Peroxymonosulfate Process under Acidic Conditions: The Overlooked Rapid Oxidation Stage, *Environ. Sci. Technol.*, 2021, **55**, 15390–15399.
11 B. Balci, M. A. Oturan, N. Oturan and I. Sirés, Decontamination of Aqueous Glyphosate, (Aminomethyl) phosphonic Acid, and Glufosinate Solutions by Electro-Fenton-like Process with Mn^{2+} as the Catalyst, *J. Agric. Food Chem.*, 2009, **57**, 4888–4894.
12 D. Feng, A. Soric and O. Boutin, Treatment technologies and degradation pathways of glyphosate: A critical review, *Sci. Total Environ.*, 2020, **742**, 140559.
13 X. Zha, X. Hou, Q. Li, H. Nan, F. Ge, Y. Liu, F. Li, D. Zhang and J. Tian, Loading Glyphosate in Attapulgite and Sodium Alginate Hydrogels to Construct pH-Responsive Controlled Release Microsphere for Enhanced Soil Sustained Release, *ACS Agric. Sci. Technol.*, 2022, **2**, 1090–1100.
14 D. P. Jaisi, H. Li, A. F. Wallace, P. Paudel, M. Sun, A. Balakrishna and R. N. Lerch, Mechanisms of Bond Cleavage during Manganese Oxide and UV Degradation of Glyphosate: Results from Phosphate Oxygen Isotopes and Molecular Simulations, *J. Agric. Food Chem.*, 2016, **64**, 8474–8482.
15 L. Jin, Y. Huang, H. Liu, L. Ye, X. Liu and D. Huang, Efficient treatment of actual glyphosate wastewater via non-radical Fenton-like oxidation, *J. Hazard. Mater.*, 2024, **463**, 132904.
16 V. E. C. da Silva, Y. S. Tadayozzi, F. F. Putti, F. A. Santos and J. C. Forti, Degradation of commercial glyphosate-based herbicide via advanced oxidative processes in aqueous media and phytotoxicity evaluation using maize seeds, *Sci. Total Environ.*, 2022, **840**, 156656.
17 L. Chen, J. Hu, A. G. L. Borthwick, W. Sun, H. Zhang, D. Jia and W. Liu, Solar-light-activated periodate for degradation and detoxification of highly toxic 6PPD-quinone at environmental levels, *Nat. Water*, 2024, **2**, 453–463.
18 Y. Guan, Z. Liu, N. Yang, S. Yang, L. E. Quispe-Cardenas, J. Liu and Y. Yang, Near-complete destruction of PFAS in

aqueous film-forming foam by integrated photo-electrochemical processes, *Nat. Water*, 2024, **2**, 443–452.

19 H. Wang, Q. Zhao, D. Li, Z. Zhang, Y. Liu, X. Guo, X. Li, Z. Liu, L. Wang, J. Ma and H. He, Boosting Photothermocatalytic Oxidation of Toluene Over Pt/N-TiO_2: The Gear Effect of Light and Heat, *Environ. Sci. Technol.*, 2024, **58**, 7662–7671.

20 Z. Tahmasebi, M. M. Momeni, A. N. Chermahini and B.-K. Lee, The improvement of photocatalytic activity of $BiVO_4$ modified with $Co(OH)_2$ nanoflake arrays for photocatalytic and photo-electrocatalytic desulfurization, *J. Alloys Compd.*, 2024, **976**, 173295.

21 M. M. Momeni and Z. Tahmasebi, Etching time effect on morphological, optical and photoelectrochemical properties of $BiVO_4$ electrodeposited films, *Inorg. Chem. Commun.*, 2022, **139**, 109300.

22 Z. Tahmasebi, M. M. Momeni and A. N. Chermahini, Enhanced $BiVO_4$ photocatalytic and photoelectrocatalytic oxidative desulfurization performance via electrodeposited copper oxide nanoparticles, *Appl. Phys. A*, 2023, **129**, 212.

23 N. Yang, Z. Yin, Z. Chen, C. Gao, Z. Cao, Y. Zheng, Z. Pan, H. Cao, S. Ye and Y. Xiong, Solar-Driven Massive Production of Dimerized Imine in Aqueous Phase via an Atomically Engineered Photocatalyst, *Angew. Chem., Int. Ed.*, 2025, e202502202.

24 T. Takata, J. Jiang, Y. Sakata, M. Nakabayashi, N. Shibata, V. Nandal, K. Seki, T. Hisatomi and K. Domen, Photocatalytic water splitting with a quantum efficiency of almost unity, *Nature*, 2020, **581**, 411–414.

25 R. Li, H. Han, F. Zhang, D. Wang and C. Li, Highly efficient photocatalysts constructed by rational assembly of dual-cocatalysts separately on different facets of $BiVO_4$, *Energy Environ. Sci.*, 2014, **7**, 1369–1376.

26 A. S. Correa, L. G. Rabelo, W. S. Rosa, N. Khan, S. Krishnamurthy, S. Khan and R. V. Gonçalves, Interfacial band alignment and photoelectrochemical properties of all-sputtered $BiVO_4$/$FeNiO_x$ and $BiVO_4$/$FeMnO_x$ p–n heterojunctions, *Energy Adv.*, 2023, **2**, 123–136.

27 N. Khan, A. Koche, H. A. Centurion, L. Rabelo, J. Bettini, G. T. dos Santos, F. L. Souza, R. V. Gonçalves and S. Khan, Triggering Synergy between p-Type Sputter-Deposited $FeMnO_x$ or $FeNiO_x$ and W-Doped $BiVO_4$ for Enhanced Oxygen Evolution, *ACS Appl. Energy Mater.*, 2024, **7**, 2129–2141.

28 X. Li, J. Zhu and H. Li, Influence of crystal facets and F-modification on the photocatalytic performance of anatase TiO_2, *Catal. Commun.*, 2012, **24**, 20–24.

29 J. Jiang, K. Zhao, X. Xiao and L. Zhang, Synthesis and Facet-Dependent Photoreactivity of BiOCl Single-Crystalline Nanosheets, *J. Am. Chem. Soc.*, 2012, **134**, 4473–4476.

30 L. Wang, J.-C. Zhou, Z.-H. Li, X. Zhang, K. M. Y. Leung, L. Yuan and G.-P. Sheng, Facet-Specific Photocatalytic Degradation of Extracellular Antibiotic Resistance Genes by Hematite Nanoparticles in Aquatic Environments, *Environ. Sci. Technol.*, 2023, **57**, 21835–21845.

31 R. Li, F. Zhang, D. Wang, J. Yang, M. Li, J. Zhu, X. Zhou, H. Han and C. Li, Spatial separation of photogenerated electrons and holes among {010} and {110} crystal facets of $BiVO_4$, *Nat. Commun.*, 2013, **4**, 1432.

32 Y. Hermans, C. Olivier, H. Junge, A. Klein, W. Jaegermann and T. Toupance, Sunlight Selective Photodeposition of $CoO_x(OH)_y$ and $NiO_x(OH)_y$ on Truncated Bipyramidal $BiVO_4$ for Highly Efficient Photocatalysis, *ACS Appl. Mater. Interfaces*, 2020, **12**, 53910–53920.

33 T. Guo, L. Jiang, K. Wang, Y. Li, H. Huang, X. Wu and G. Zhang, Efficient persulfate activation by hematite nanocrystals for degradation of organic pollutants under visible light irradiation: Facet-dependent catalytic performance and degradation mechanism, *Appl. Catal., B*, 2021, **286**, 119883.

34 C. Wang, W. Li, Z. Zhang, D. Lei, G. Che, C. Gou, J. Zhang and Z. Hao, A novel iron sulfide phase with remarkable hydroxyl radical generation capability for contaminants degradation, *Water Res.*, 2024, **251**, 121166.

35 L. Yang, Z. Chen, Q. Cao, H. Liao, J. Gao, L. Zhang, W. Wei, H. Li and J. Lu, Structural Regulation of Photocatalyst to Optimize Hydroxyl Radical Production Pathways for Highly Efficient Photocatalytic Oxidation, *Adv. Mater.*, 2024, **36**, 2306758.

36 A. S. Santos, P. J. T. Ferreira and T. Maloney, Bio-based materials for nonwovens, *Cellulose*, 2021, **28**, 8939–8969.

37 J. Deng, F. Li, Z. Qi, W. Huang, Z. Wan, L. Zhang, D. Zheng, G. Li and F. Zhang, A novel redox synergistic mechanism of peroxymonosulfate activation using Pd-Fe_3O_4 for ultra-fast chlorinated hydrocarbon degradation, *Appl. Catal., B*, 2024, **359**, 124499.

38 M. H. Urgesa, D.-H. Kuo, T. N. Gemeda, Q.-N. Ha and N. S. Gultom, Ambient NN bond weakening hydrogenation by utilizing the highly defective Cu_3BiS_3/MnO_2 electrocatalyst for ammonia yield above 3 mg/h cm^2: The N2-nano dipole interaction micromechanism, *Appl. Catal., B*, 2024, **355**, 124194.

39 E. S. Ilton, J. E. Post, P. J. Heaney, F. T. Ling and S. N. Kerisit, XPS determination of Mn oxidation states in Mn (hydr)oxides, *Appl. Surf. Sci.*, 2016, **366**, 475–485.

40 T. Liu, Z. Pan, J. J. M. Vequizo, K. Kato, B. Wu, A. Yamakata, K. Katayama, B. Chen, C. Chu and K. Domen, Overall photosynthesis of H_2O_2 by an inorganic semiconductor, *Nat. Commun.*, 2022, **13**, 1034.

41 T. Ghosh, M. B. Vukmirovic, F. J. DiSalvo and R. R. Adzic, Intermetallics as Novel Supports for Pt Monolayer O_2 Reduction Electrocatalysts: Potential for Significantly Improving Properties, *J. Am. Chem. Soc.*, 2010, **132**, 906–907.

42 N. Yang, S. Zhang, Y. Xiao, Y. Qi, Y. Bao, P. Xu, S. Jin and F. Zhang, Insight into the Key Restriction of $BiVO_4$ Photoanodes Prepared by Pyrolysis Method for Scalable Preparation, *Angew. Chem., Int. Ed.*, 2023, **62**, e202308729.

43 Y. Sheng, I. A. Abreu, D. E. Cabelli, M. J. Maroney, A.-F. Miller, M. Teixeira and J. S. Valentine, Superoxide Dismutases and Superoxide Reductases, *Chem. Rev.*, 2014, **114**, 3854–3918.

44 F. Puga, J. A. Navío and M. C. Hidalgo, A critical view about use of scavengers for reactive species in heterogeneous photocatalysis, *Appl. Catal., A*, 2024, **685**, 119879.

45 J. Li, X. Liu, Y. Zheng, Z. Cui, H. Jiang, Z. Li, S. Zhu and S. Wu, Achieving Fast Charge Separation by Ferroelectric Ultrasonic Interfacial Engineering for Rapid Sonotherapy of Bacteria-Infected Osteomyelitis, *Adv. Mater.*, 2023, **35**, 2210296.

46 Y. Wang, R. Zhang, P. Zang, R. Zhao, L. Wu, Y. Zhu, D. Yang, S. Gai and P. Yang, Synergizing Pyroelectric Catalysis and Enzyme Catalysis: Establishing a Reciprocal and Synergistic Model to Enhance Anti-Tumor Activity, *Adv. Mater.*, 2024, **36**, 2401111.

47 C. Cao, H. Zou, N. Yang, H. Li, Y. Cai, X. Song, J. Shao, P. Chen, X. Mou, W. Wang and X. Dong, Fe_3O_4/Ag/Bi_2MoO_6 Photoactivatable Nanozyme for Self-Replenishing and Sustainable Cascaded Nanocatalytic Cancer Therapy, *Adv. Mater.*, 2021, **33**, 2106996.

48 Y. Qi, B. Zhang, G. Zhang, Z. Zheng, T. Xie, S. Chen, G. Ma, C. Li, K. Domen and F. Zhang, Efficient overall water splitting of a suspended photocatalyst boosted by metal-support interaction, *Joule*, 2024, **8**, 193–203.